Seventh International Conference on
Computational Fluid Dynamics (ICCFD7),
Big Island, Hawaii, July 9-13, 2012

ICCFD7-2302

Direct numerical simulation of particle dispersion in a spatially developing turbulent boundary layer

M. S. Dodd*, K. Webster* and A. Ferrante**
Corresponding author: ferrante@aa.washington.edu

* Ph.D. Student, Aeronautics & Astronautics, University of Washington, Seattle, USA.
** Assistant Professor, Aeronautics & Astronautics, University of Washington, Seattle, USA.

Abstract: We have performed direct numerical simulation (DNS) of a particle-laden spatially developing, zero-pressure-gradient turbulent boundary layer at $\text{Re}_\theta = 1000 - 2750$. We computed the Lagrangian trajectories of fluid points and solid particles of three different Stokes numbers (St $= 0.1$, 1, and 5). The particles were released in the computational domain from a line source at three different distances from the wall, in the viscous sublayer, the buffer layer, and the log-layer ($z_{inj}^+ = 2$, 10, and 100). The fluid points mean-displacement obtained from the DNS is analyzed and compared to the theory of Batchelor (1964). Also, the time development of fluid point and solid particle mean-square displacement (or dispersion) and turbulent diffusivity are analyzed. Dispersion statistics are generally found to be strongly influenced by particle inertia. Such dependence is mostly caused by the particles tendency to preferentially concentrate in the viscous sublayer. Furthermore, for very long times (several integral timescales), the DNS results show that the streamwise dispersion of fluid points and particles with St$= 0.1$ is nearly $\propto t^{5/3}$, while that of particles with St$= 1$ and 5 is nearly $\propto t^{5/2}$. For all cases studied, the long-time wall-normal dispersion is nearly $\propto t$.

Keywords: Direct Numerical Simulation, Turbulent Boundary Layers, Particle-Laden Flows, Dispersion.

1 Introduction

Particle dispersion in turbulent flows is common in many engineering and environmental applications. Fundamental understanding of particle dispersion in turbulent flows can improve prediction of sedimentation processes and pollutant dispersion in the atmosphere. A review on dispersion in homogeneous turbulent flows is given by Yeung (2002). Theoretical studies of fluid points dispersion have been performed for isotropic turbulence by Taylor (1921), for homogeneous shear flow by Corrsin (1959), and for turbulent boundary layers by Batchelor (1964) and Chatwin (1968). These theories rely on the turbulent diffusivity hypothesis.

Practical flows are mostly inhomogeneous turbulent flows, and often bounded by one or more walls. Soldati & Marchioli (2009) review the DNS studies of particle-laden fully-developed turbulent channel flows with emphasis on particle deposition and entrainment. DNS studies of particle dispersion in the zero-pressure-gradient spatially developing turbulent boundary layer, which is homogeneous only in the spanwise direction, have not been reported in the refereed literature.

One of the first experiments on dispersion in a turbulent boundary layer was conducted by Poreh & Cermak (1964), in which ammonia gas was released steadily from a line source near the wall. They identified four stages of dispersion in their experiments, and Shlien & Corrsin (1976) identified similar stages when measuring mean temperature profiles behind a heated "tagging" wire in a turbulent boundary layer:

1. An initial stage when the particles exhibit short time ($t \ll T_\text{L}$, where T_L is the Lagrangian integral time scale of turbulence) dispersion behavior near the source, in which the particle distribution is approximately Gaussian.

2. An intermediate stage in which the dispersed cloud is "submerged in the boundary layer", i.e., particles are within the turbulent boundary layer and below the *viscous superlayer*, a thin front separating the turbulent boundary layer fluid from the irrotational free-stream fluid (see e.g. Pope (2000)).

3. A transition stage when the viscous superlayer acts as a "lid" which inhibits dispersion. Dispersion in the irrotational region is greatly attenuated as it is only accomplished through the much slower process of molecular diffusion.

4. A final (asymptotic) stage in which the particle dispersion is regulated by the growth of the spatially developing boundary layer. The dispersed cloud is contained between the wall and the viscous superlayer, and mean-profiles become independent of the line-source distance from the wall.

The clustering of particles near the wall, commonly referred to as turbophoresis (Caporaloni *et al.*, 1975), has been documented, e.g., Reeks (1983) and Marchioli & Soldati (2002). Turbophoresis has been described as a process whereby inertial particles in turbulent flows preferentially migrate to regions of lower turbulence intensity. Recent direct numerical simulations of inertial particle dispersion in fully-developed turbulent channel flow have revealed that coherent structures play a dominant role in transferring particles to the wall (Marchioli & Soldati, 2002). Additionally, particle Stokes number are found to affect the peak concentration magnitude.

Our objective in the current paper is to present, for the first time, DNS results of dispersion of fluid points and solid particles from a line source in a spatially developing turbulent boundary layer. We identify the effects of particle Stokes number and release distance from the wall on particle statistics and we compare fluid point dispersion with the theory of Batchelor (1964).

2 Mathematical Description

2.1 Governing Equations

The governing equations for an incompressible turbulent boundary layer flow are the three-dimensional unsteady Navier-Stokes equations, which are given here in dimensionless form:

$$\frac{\mathrm{D}U_j}{\mathrm{D}t} = - \frac{\partial p}{\partial x_j} + \nu \frac{\partial^2 U_j}{\partial x_k \partial x_k} , \tag{1}$$

and the continuity equation,

$$\frac{\partial U_j}{\partial x_j} = 0 , \tag{2}$$

where x_j are the streamwise x-, spanwise y- and wall-normal z-direction respectively for $j = 1, 2, 3$. The dimensionless kinematic viscosity is $\nu = 1/\mathrm{Re}_\delta$ where $\mathrm{Re}_\delta = \tilde{U}_\infty \tilde{\delta}_0/\tilde{\nu}$ is the Reynolds number based on the dimensional free-stream velocity $\tilde{U}_\infty$, the dimensional boundary layer thickness (based on the location of 99% of the freestream velocity) $\tilde{\delta}_0$ at the inlet plane ($x = 0$) of the computational domain, and the dimensional kinematic viscosity $\tilde{\nu}$ ($= 10^{-6}\mathrm{m}^2\mathrm{s}^{-1}$). All variables in (1) and (2) are non-dimensionalized by $\tilde{U}_\infty$ and $\tilde{\delta}_0$ (Table 1).

Throughout the paper, dimensionless quantities in wall-units carry the superscript '$+$', i.e. $U_{ref}^+ = U_{ref}/u_\tau$ and $z^+ = zu_\tau/\nu$ where $u_\tau = \sqrt{\tau_w/\rho_f}$ is the friction velocity, τ_w is the wall shear stress, and ρ_f is the fluid density. Additionally, the fluid velocity component U_i is written as the sum of its mean and fluctuation, $U_i(x, y, z, t) = \langle U_i \rangle(x, z) + u_i(x, y, z, t)$, where $\langle \ldots \rangle$ represents, spatial averaging in the spanwise (y) direction in addition to time averaging of the enclosed quantity, and u_i is the local instantaneous deviation from $\langle U_i \rangle$.

The particle equation of motion for particles smaller than Kolmogorov's length scale of turbulence, derived by Maxey & Riley (1983), can be written for large ratio (ρ_p/ρ_f) of particle density to fluid density as

$$\frac{\mathrm{d}V_j}{\mathrm{d}t_p} = \frac{(U_j - V_j)}{\tau_p} f_d(Re_p) \tag{3}$$

2

where d/dt_p is the time derivative following the moving particle, V_j is the instantaneous particle velocity, U_j is the instantaneous fluid velocity at the particle location, and $f_d(\mathrm{Re}_p) = 1 + 0.15\mathrm{Re}_p^{0.687}$ is an empirical correction to Stokes formula. The particle Reynolds number is defined as $\mathrm{Re}_p = d|U_j - V_j|/\nu$. τ_p is the particle response time, which for Stokes drag law is

$$\tau_p = \frac{d^2}{18\nu}\frac{\rho_p}{\rho_f} \tag{4}$$

where d is the particle diameter.

2.2 Numerical Method

We employ the Eulerian-Lagrangian approach in which we solve the fluid continuity and momentum equations, Eqs. (1) and (2), in an Eulerian framework, whereas the particle equation of motion, Eq. (3), is solved for each particle to track its trajectory in time.

Figure 1 shows a schematic of the spatially developing turbulent boundary layer (SDTBL) flow where the line source ($x = 10.0\delta_0$) is placed downstream the inlet recycling plane ($x = 8.25\delta_0$). The computational domain is a parallelpiped whose dimensions L_x, L_y, and L_z and the corresponding number of grid points, N_x, N_y and N_z in the streamwise, spanwise and wall-normal directions respectively are listed in Table 2. The computational mesh is equispaced in the streamwise and spanwise directions, with grid spacings Δx^+ and Δy^+ (Table 2), whereas in the vertical direction, the mesh is stretched gradually via mapping a uniform computational grid ζ into its non-uniform counterpart z with a combination of hyperbolic tangent functions (Ferrante & Elghobashi, 2004) with the closest grid point to the wall located at $z_{min}^+ = 0.33$.

Re_δ	$\nu = 1/\mathrm{Re}_\delta$	$u_{\tau 0}$	$\tilde{\delta}_0$ (mm)	$\tilde{U}_\infty$(m s^{-1})
9.5×10^3	1.05×10^{-4}	0.0447	10.0	0.95

Table 1: Fluid properties.

L_x	L_y	L_z	L_x^+	L_y^+	L_z^+	N_x	N_y	N_z	Δx^+	Δy^+	z_{min}^+
$90\delta_0$	$5\delta_0$	$7.2\delta_0$	38177	2121	3053	4608	512	256	8.28	4.14	0.33

Table 2: Computational domain parameters.

The governing equations, (1) and (2), were discretized in space in an Eulerian framework on a staggered mesh using a second-order central difference scheme, except for the mean advection terms, which were evaluated via a fifth-order upwind differencing scheme. Time integration was performed via the second-order Adams-Bashforth scheme with a time step $\Delta t = 0.075\nu/u_\tau^2$. Pressure was treated implicitly and was obtained by solving the Poisson equation in finite-difference form using a cosine transform in the streamwise direction, a fast Fourier transform (FFT) in the spanwise direction, and Gauss elimination in the wall-normal direction (see Ferrante & Elghobashi (2004) for a complete description).

Particles were released gradually downstream the recycling plane from a line source located at $x = 10\delta_0$ and variable height z_{inj}^+ (Fig. 1). The particles were released over one Eulerian integral time scale ($T_{x,L} \approx 1.5$) starting at time $t = 0$ in order to improve statistical accuracy by eliminating memory effects near the source. The time a particle was released will be referred to hereinafter as "release time", $t_{p,r}$. The initial velocity at $t_{p,r}$ of each particle was set equal to the instantaneous fluid velocity at the particle position. Particle trajectories were then tracked in time by solving for each particle the particle equation of motion (Eq. (3)) using the second-order Adams-Bashforth scheme to compute the particle velocity. The fluid velocity, U_j,

Case	λ_{rfl}
1	1.25 ± 0.25
2	2.5 ± 0.5
3	5 ± 1
4	7.5 ± 1.5

Table 3: Dynamic reflection parametric study

at the particle location which is needed to solve Eq. (3), was computed via a fourth-order accurate fully three-dimensional Hermite interpolation polynomial (see Ferrante (2004), Appendix D) which switches to a one-sided scheme for particles located below the first grid point from the wall. The particle position was then computed from the time integration of the particle velocity. We tracked $N_p = 8 \times 10^6$ particles. The results (not shown) using $N_p = 17 \times 10^6$ were indistinguishable from those using $N_p = 8 \times 10^6$. Particles that hit the wall are reflected elastically into the interior of the compuational domain. The simulations were stopped after 0.001% of the particles have exited the computational domain.

2.2.1 Inflow and outflow boundary conditions

The method for generation of the turbulent flow conditions at the inlet plane ($x = 0$) are described in detail by Ferrante & Elghobashi (2004). However, in the present work, we have implemented three modifications to that methodology, in particular, regarding (i) the computational domain, (ii) the rescaling procedure, and (iii) the outflow convective velocity. Each modification is now described in detail.

(i) Computational domain Instead of using two computational domains, a short box (A, $L_x = 10\delta_0$) to generate inflow conditions and a long box (B, $L_x = 20\delta_0$) for the main simulation (see Fig. 1 of Ferrante & Elghobashi (2004)), as in Ferrante & Elghobashi (2004), we simply use a single very long box (A, $L_x = 90\delta_0$) in which we keep generating inflow conditions through the recycling procedure, thus avoiding the writing and reading operations of inflow conditions from box A to box B. Overall this saves storage and halves the computational time avoiding the need of writing and reading the inflow plane information from box A into B.

(ii) Rescaling procedure The rescaling procedure of Lund *et al.* (1998) used in Task 2 of Ferrante & Elghobashi (2004) generates spurious two-point velocity correlation,

$$R_{ij}(r, x, t) = \langle u_i(x, t) u_j(x + r, t) \rangle, \tag{5}$$

as shown in Fig. 2(a) with unphysical peak values of R_{11} at $x = 8.25\delta_0$ and $16.5\delta_0$. To remove these peaks, the rescaled plane was dynamically reflected similarly to the method in Morgan *et al.* (2011), in which the dynamic reflection was applied to a large-eddy simulation of a supersonic boundary layer. We have adapted the dynamic reflection methodology of Morgan *et al.* (2011) to DNS of SDTBL.

Due to the periodicity in the spanwise direction (y-axis), the inflow can be reflected about any y-plane to remove the non-physical peaks of the velocity correlations. A single inflow plane reflection generates a correlation in a diagonal direction. To remove this, the plane has to be reflected at random y-planes at random time intervals. Also, the period of time between the change in reflection planes has to be random to remove any time correlations.

A parametric study was performed to find the best range of the random reflection times. The parameters used to define the random reflection time interval are as follows: λ_{rfl} as defined in the paper by Morgan *et al.* (2011) as the characteristic streamwise streaks length. This is used to find the mean reflection time $\tau_{\mathrm{rfl}} = \frac{\lambda_{\mathrm{rfl}}}{0.8 U_\infty}$. Case 3 of the test-cases summarized in Table 3 produced the best results by removing the spurious velocity correlations as shown in Fig. 2(b) and by producing accurate results (Figs. 4 5).

(iii) Outflow convective velocity At the outflow plane ($x = L_x$), a zero-pressure gradient in the streamwise direction ($\partial p / \partial x = 0$), and the following convective condition Lowery & Reynolds (1986) was imposed

for the velocity fluctuations,

$$\frac{\partial u_j}{\partial t} + U_c \frac{\partial u_j}{\partial x} = 0,$$ (6)

where U_c is the convective velocity at the exit plane and u_j is the fluctuating velocity. The convective velocity in Ferrante & Elghobashi (2004) was defined by taking the span and wall normal averaged convective velocity:

$$U_C(t) = \langle\langle U_C(x,y,z,t)\rangle_y\rangle_z.$$ (7)

The new outflow convective velocity is only averaged in the spanwise direction:

$$U_C(z,t) = \langle U_C(x,y,z,t)\rangle_y.$$ (8)

Using (7) instead of (8) in (6) allows to advect the velocity fluctuations at the outflow plane at their local average velocity, rather then a plane-averaged speed that would be too large for the advection at the near wall grid points. This modification improves the spatial development of the boundary layer near the outflow plane by producing a nearly straight line of the $\mathrm{Re}_\theta(x)$ profile as shown in Fig. 3.

3 Results

3.1 SDTBL

We now compare our DNS results with experimental and DNS data for a spatially developing turbulent boundary layer over a flat plate at $\mathrm{Re}_\theta = 1430$ and 2541. Figures 4(a) and (b) display the comparison in wall units for the mean streamwise velocity, $\langle U_1 \rangle^+$, and three Reynolds stresses at $\mathrm{Re}_\theta = 1430$ ($x = 21.8\delta_0$) with the experimental data of DeGraaff & Eaton (2000) and the DNS results at $\mathrm{Re}_\theta = 1421$ of Schlatter & Örlü (2010). Figures 4(a) and (b) show similar agreement between the present DNS and the DNS by Schlatter & Örlü (2010). The mean velocity profile is in excellent agreement with the experimental profile. The Reynolds stresses also show good agreement with the experimental data. Figures 5(a) and (b) display the comparison of $\langle U_1 \rangle^+$ and $\langle u_1^2 \rangle^+$ at $\mathrm{Re}_\theta = 2541$ ($x = 83.0\delta_0$) with the experimental data of Schlatter $et\ al.$ (2009) and DNS data of Schlatter & Örlü (2010). Again, $\langle U_1 \rangle^+$ of the present DNS is in excellent agreement with the experimental profile. Figure 5(b) shows a similar discrepancy in the $\langle u_1^2 \rangle^+$ max value between the present DNS and the DNS of Schlatter & Örlü (2010) compared with their experiments. Our computed skin friction coefficient ($C_{fx} = 2\tau_w/(\rho U_\infty^2) = 3.93 \times 10^{-3}$ and 3.40×10^{-3}, where $\tau_w = \mu[\partial_z \langle U_1 \rangle(x,z)]_{z=0}$) at $\mathrm{Re}_\theta = 1430$ and $\mathrm{Re}_\theta = 2541$ are nearly identical to those measured ($C_{fx} = 3.96 \times 10^{-3}$ and 3.39×10^{-3}) by DeGraaff & Eaton (2000) and Schlatter $et\ al.$ (2009), respectively.

3.2 Particle parameters

We studied four cases to understand how particles of different Stokes number ($\mathrm{St}= \tau_p/\tau_k$) disperse in a SDTBL. The particle properties are shown in Table 4. Case A represents the fluid points, and cases B, C, and D represent particle-laden flows with different particle Stokes numbers in zero gravity, $\mathrm{St}= 0.1$, 1.0, and 5.0, respectively. The value for the reference Kolmogorov time scale (τ_k) and length scale (η) were computed at $x = 10\delta_0$ and $z^+ = 10$, and found to be $\tau_k = 0.137$ and $\eta = 0.00377$. We only changed the particle diameter for each case to change the particle response time, τ_p. Figure 6 shows the Stokes number dependence on z^+, at three streamwise locations for cases B, C, and D. Throughout the paper particle case identifiers are appended with a number corresponding to the particle injection height, z_{inj}^+, e.g., case B100 represents $\mathrm{St}= 0.1$ particles released from $z_{inj}^+ = 100$. The values of $\tilde{d}$ in Table 4 were computed using the dimensional values of $\tilde{\delta}_0$ and $\tilde{U}_\infty$ in Table 1.

3.3 Time scales of SDTBL

Table 5 provides a summary of the time scales that were computed from the fluid point velocities (case A10 and A100) and from the turbulent flow velocity at the line source. The Eulerian integral time scale was

Case	St$=\tau_p/\tau_k$	τ_p	τ_p^+	d	d^+	d/η	$\tilde{d}(\mu\mathrm{m})$	ρ_p/ρ_f	$\mathrm{Re}_{p,max}$
A	0	0	0	0	0	0	0	1	0
B	0.1	0.014	0.27	1.609×10^{-4}	0.069	0.043	1.61	1000	0.38
C	1.0	0.137	2.68	5.087×10^{-4}	0.220	0.135	5.09	1000	2.52
D	5.0	0.683	13.42	1.138×10^{-3}	0.492	0.302	11.38	1000	7.34

Table 4: Particle properties at injection time ($t = 0$).

computed from the two-time Eulerian velocity autocorrelation function as

$$R_{i,\mathrm{E}}(\tau) = \frac{\langle u_i(t_0) u_i(t_0 + \tau) \rangle}{\langle u_i(t_0)^2 \rangle}, \tag{9}$$

where averaging, $\langle \ldots \rangle$, is performed in both the spanwise and streamwise direction. The Eulerian integral time scale is then defined as

$$T_{i,\mathrm{E}} = \int_0^\infty R_{\mathrm{E},i}(\tau)\mathrm{d}t. \tag{10}$$

The Lagrangian autocorrelation function can also be written as

$$R_{i,\mathrm{L}}(\tau) = \frac{\langle v_i(t_0) v_i(t_0 + \tau) \rangle_{N_p}}{[\langle v_i(t_0)^2 \rangle_{N_p}]^{\frac{1}{2}} [\langle v_i(t_0 + \tau)^2 \rangle_{N_p}]^{\frac{1}{2}}}, \tag{11}$$

where $v_i(t)$ is the fluid point velocity and $\langle \ldots \rangle_{N_p}$ denotes the ensemble average of the enclosed quantity over the total number of particles, N_p. The Lagrangian integral time scale is then defined as

$$T_{i,\mathrm{L}} = \int_0^\infty R_{\mathrm{L},i}(\tau)\mathrm{d}t. \tag{12}$$

z_{inj}^+	τ_k $(x = 10\delta_0)$	$T_{x,\mathrm{E}}$	$T_{x,\mathrm{L}}$
10	0.0137	1.156	1.758
100	0.0351	1.532	1.850

Table 5: Fluid point properties and flow parameters.

3.4 Particle mean displacement

The particle mean displacement in the x_i-direction of dispersed particles is given by

$$\langle x_{i,p}(t^*) \rangle_{N_p} = \frac{1}{N_p} \sum_{k=1}^{N_{\mathrm{inj}}} \sum_{j=1}^{N_{p,k}} [x_{i,p}(t^*) - x_{i,p}(t_{p,r})]_{j,k} \tag{13}$$

where $x_{i,p}(t^*)$ is the particle location, $t_{p,r}$ is the time at which the particle is released, t^* is a reference time used for computing particle statistics defined as $t^* \equiv t - t_{p,r}$, N_{inj} is the number of particle injection events, $N_{p,k}$ is the number of particles injected at each injection event, and N_p is the total number of particles tracked in the computational domain:

$$N_p = N_{\mathrm{inj}} N_{p,k}. \tag{14}$$

3.4.1 Comparison with Batchelor's (1964) theory

Using a Lagrangian similarity hypothesis, Batchelor (1964) derived analytical expressions for the displacement of a passive scalar (fluid point) in the log-law region. The hypothesis is that "the statistical properties of the velocity of a marked fluid particle at time t after release from the ground depend only on u_τ and t." Batchelor extended the hypothesis to include particle sources above the ground. This extension is: "the statistical properties of the velocity of a marked particle at time t after release at height z_{inj} are the same as those of a particle released at the ground at the instant t_1, provided $t \gg t_1$, where t_1 is expected to be of the order of magnitude of the time scale of turbulence at height z_{inj}, that is, of order z_{inj}/u_τ." Batchelor then derived formulas for the mean streamwise and wall-normal displacement of fluid points:

$$\langle z_p(t) \rangle_{N_p} = b u_\tau t \tag{15}$$

$$\langle x_p(t) \rangle_{N_p} = \frac{c \langle z_p(t) \rangle_{N_p}}{b\kappa} \left[\log\left(\frac{c \langle z_p(t) \rangle_{N_p}}{z_0} \right) - 1 \right] \tag{16}$$

where b and c are constants taken to be 0.41 and 0.5615 respectively, κ is von Kármán's constant, and z_0 is the length characterizing the surface roughness. For smooth walls, Cermak (1963) suggests $z_0 = 0.141(\nu/u_\tau)$.

Figure 7 shows the time development of the streamwise and wall-normal mean displacement of fluid points from present DNS and Batchelor's (1964) theory (Eqs. (15) and (16)). In Fig. 7, Batchelor's (1964) condition that $t_1 = \mathcal{O}(z_{inj}/u_\tau)$ is shown by the vertical dashed line. Also, in Fig. 7, we have added a blue area for which the lower limit is at $t = T_{x,L} = 1.80$ for fluid points released at $z_{inj}^+ = 50$, and the upper limit corresponds to the time when 35% of the fluid points have exited the log-layer. Over the period indicated by the blue area, Batchelor's theory is in excellent agreement with our DNS results.

3.4.2 Solid particles

Figure 8 shows the time development of $\langle x_p(t^*) \rangle_{N_p}$ for the four cases (A-D) initially released in the log-layer at $z^+ = 100$, the buffer layer at $z^+ = 10$, and the viscous sublayer at $z^+ = 2$. The quantity $\langle x_p(t^*) \rangle_{N_p}$ is the centroid location of the particle cloud in the x-direction at time t^*. In all cases, the mean streamwise displacement of the cloud decreases for increasing Stokes number. Also, this effect is enhanced as the injection height z_{inj}^+ is decreased. For $z_{inj}^+ = 100$, Fig. 8(a) shows that at $t^* = 80$ the centroid of the particles with St= 5 (case D) has traveled 21% less distance than that of the fluid points (case A), whereas, for $z_{inj}^+ = 2$, Fig. 8(c) shows that this difference increases to 59%. Furthermore, Fig. 8(a) ($z_{inj}^+ = 100$) shows that the centroid streamwise displacement is $\propto t$, thus the centroid moves at approximately constant streamwise velocity as shown in Fig. 8(a).

Figure 9 shows the time development of the streamwise velocity of the particle cloud centroid, $\frac{d}{dt^*}\langle x_p(t^*) \rangle_{N_p}$. For all z_{inj}^+, $\frac{d}{dt^*}\langle x_p(t^*) \rangle_{N_p}$ decreases for increasing particle Stokes number. Figure 9(a) ($z_{inj}^+ = 100$) shows that particle cloud centroid of cases A, B, and C travels with constant streamwise velocity for $t^* > 70$. Also, in case D100 (St= 5), $\frac{d}{dt^*}\langle x_p(t^*) \rangle_{N_p}$ decreases in time, i.e., the particle cloud centroid is decelerating. For that case, simulation in a longer computational domain would be needed to show the asymptotic streamwise velocity of the cloud centroid. Figures 9(b) and (c) show that the particle cloud centroid initially after injection undergoes a transient phase lasting approximately one Lagrangian integral time scale ($T_{x,L}$), and then has a period of increasing $\frac{d}{dt^*}\langle x_p(t^*) \rangle_{N_p}$ lasting several integral timescales before reaching a steady value of the mean streamwise velocity. The steady streamwise mean velocity of the centroid is reached only in cases A, B and C for $z_{inj}^+ = 100$. In all other cases, such behavior cannot be observed in the present results because longer time statistics would be needed, thus a longer computational domain. Figure 9(c) shows that the centroid of particles with St= 5 approach constant velocity when $z_{inj}^+ = 2$ and that $\frac{d}{dt^*}\langle x_p(t^*) \rangle_{N_p}$ is roughly 75% less than the final velocity of the fluid point cloud centroid at $t^* = 80$.

Particles disperse in the boundary layer after they have been released from the line source. Particles in cases A, B (St=0 and 0.1) do not preferentially accumulate as shown by the nearly uniform concentration profile of the particles A and B in Fig. 10,, and, when released in a region of local mean velocity closer to the average velocity of the cloud, they reach their asymptotic streamwise centroid velocity in a shorter time than when released near the wall (Fig. 9). For increasing Stokes number preferential accumulation in the

near-wall region increases (turbophoresis), as shown in Fig. 10, thus the surrounding mean fluid velocity to the particles decreases, and consequently the asymptotic centroid velocity decreases (Fig. 9). Particles in case D, preferentially accumulate in the viscous sublayer independently from the injection height (Fig. 10). The asymptotic centroid velocity is reached in case D2 for $t^* > 50$ because the particles are released in the viscous sublayer where they preferentially accumulate, but as the injection height increases the time required for the particles in case D to reach the asymptotic velocity increases due to the fact that longer time is required for the particles to preferentially accumulate farther from their injection location in the viscous sublayer.

To understand the time evolution of particle accumulation in the wall region, the number of particles in the viscous sublayer ($0 < z^+ < 5$) was counted and then normalized by the total number of particles in the computational domain, $N_{p,\nu}(t)/N_p$. Figure 11 shows that independent of the injection height, $N_{p,\nu}(t)/N_p$ increases with Stokes number. Figure 11(c) shows the fluid points (case A) and the particles at St=0.1 (case B) are nearly all ejected from the viscous sublayer for long times. In stark contrast, the largest particles (case D) approach an equilibrium concentration of roughly 80% in this region. Hence, the mean displacement of large particles is greatly reduced as a majority are trapped in the relatively stagnant viscous sublayer, whereas small particles and fluid points show a net flux into the higher speed outer flow. Figure 11(a) and (b) show that particles released outside the viscous sublayer also preferentially concentrate near the wall and this effect is again accentuated for increasing Stokes number. Furthermore, an equilibrium state is reached for all but the St= 5 particles. The equilibrium state appears to be dependent on the release height z_{inj}^+, however, a longer domain is needed to verify this.

Figure 12 shows the time development of the vertical position of the particle-cloud centroid in wall units, $\langle z_p^+(t^*)\rangle_{N_p}$. For all z_{inj}^+, $\langle z_p^+(t^*)\rangle_{N_p}$ decreases for increasing particle Stokes number from case A to case D, because as the Stokes number increases the particle cloud center of mass is closer to the wall (Fig. 10). This effect is also enhanced as z_{inj}^+ is decreased because the instantaneous particle concentration near the wall is higher when particles are released near the wall (Fig. 10). In fact, for $z_{inj}^+ = 100$, Fig. 12(a) shows that at $t^* = 80$, $\langle z_p^+(t^*)\rangle_{N_p}$ in case D is 40% smaller than that in case A, whereas, for $z_{inj}^+ = 2$, Fig. 12(c) shows that this difference increases to 82%.

Figure 13 shows the time development of the wall-normal velocity of the particle cloud centroid, $\frac{d}{dt^*}\langle z_p^+(t^*)\rangle_{N_p}$. For all z_{inj}^+, $\frac{d}{dt^*}\langle z_p^+(t^*)\rangle_{N_p}$ decreases for increasing particle Stokes number. Figures 13(a) and (b) show the centroid experiences a period of rapid acceleration in the wall-normal direction lasting roughly 2 $T_{x,\mathrm{L}}$, then a short period of nearly constant maximum velocity, followed by an extended period of deceleration in which for long times ($t^* > 70$) constant wall-normal velocity is approached. Figure 13(c) shows for all cases (A-D), for $z_{inj}^+ = 2$, $\frac{d}{dt^*}\langle z_p^+(t^*)\rangle_{N_p}$ increases significantly more slowly than in Figs. 13(a) and (b). Finally, the $\frac{d}{dt^*}\langle z_p^+(t^*)\rangle_{N_p}$ peak decreases for decreasing z_{inj}^+ independent of particle Stokes number.

3.5 Particle mean-square displacement

The particle mean-square displacement (or dispersion), σ_i^2, of an ensemble of dispersed particles in the x_i-direction is defined and calculated as

$$\sigma_i^2(t^*) \equiv \left\langle (x_{i,p}(t^*) - \langle x_{i,p}(t^*)\rangle)^2 \right\rangle_{N_p} = \frac{1}{N_p}\sum_{k=1}^{N_{\mathrm{inj}}}\sum_{j=1}^{N_{p,k}}\left[x_{i,p}(t^*) - \langle x_{i,p}(t^*)\rangle\right]_{j,k}^2, \tag{17}$$

which is a measure of the particle-cloud spreading about its center of mass.

Figure 14 shows the time development of the particle dispersion in the streamwise direction, $\sigma_x^2(t^*)$. For $z_{inj}^+ = 10$ and 100, $\sigma_x^2(t^*)$ increases with the Stokes number from case A to D because the spreading rate is enhanced by the significant number of particles trapped in the slow motion of the viscous sublayer (Fig. 11). For $z_{inj}^+ = 2$ instead $\sigma_x^2(t^*)$ is not monotone with the Stokes number and is maximum in case C (St=1). Figures 15 and 16 show instantaneous color contours of the number of particles summed in the spanwise direction for cases A100 and D100, respectively, at times $t = 0.8 \ldots 78.4$. Also shown is the the boundary layer thickness, $\delta(x)$, (solid white line) and the lower and upper boundaries of the log layer (dashed white lines). Figure 15 shows that the fluid point cloud released at $z_{inj}^+ = 100$ is increasingly sheared in the streamwise direction in time. Also, the white line, $\delta(x)$, limits the growth of the cloud in the wall-normal

direction, however particles can still be advected beyond $\delta(x)$ by intermittent *large eddies*, as $\delta(x)$ is the boundary layer thickness of the mean flow. Figure 16 shows the cloud with St= 5 particles obtains a peak concentration at $x \approx 12.5\delta_0$ (see inset) in the viscous sublayer which is approximately fixed in time. We see in general, much higher particle concentrations near the wall and much lower particle concentrations in the outer flow compared to fluid points (case A100). In all cases C and D, (not shown) particles separate into two clouds, one trapped in the viscous sublayer (see inset of Fig. 16) and one traveling in the outer flow, whereas in cases A and B particles are more uniformly distributed across the boundary layer as shown in Fig. 10 and 15.

For fluid points and particles with St= 0.1, and $t^* > 70$, Fig. 14 (in log scaling) shows σ_x^2 is nearly $\propto t^{5/3}$. Surprisingly, this result for the streamwise mean-square displacement in the SDTBL is markedly different from that in homogeneous turbulent shear flows where for long times ($t \gg T_{\rm L}$) $\sigma_x^2 \propto t^3$, which was shown theoretically by Corrsin (1959) and using DNS by Ahmed & Elghobashi (2001).

Figure 17 shows the time development of the particle dispersion in the wall-normal direction, $\sigma_z^2(t^*)$. For $z_{inj}^+ = 100$, $\sigma_z^2(t^*)$ is nearly independent of the particle Stokes number. Decreasing the injection wall-normal distance from $z_{inj}^+ = 100$ to 10 and to 2, $\sigma_z^2(t^*)$ decreases for all cases. For $z_{inj}^+ = 2$, $\sigma_z^2(t^*)$ decreases with the Stokes number from cases A & B to D. Finally, for all cases, $\sigma_z^2(t^*)$ is approximately $\propto t$ for $t^* > 30$.

3.6 Particle turbulent diffusivity

The dispersion can be expressed for all times in terms of a diffusivity, $\hat{\Gamma}_{i,{\rm T}}(t^*)$ defined as:

$$\hat{\Gamma}_{i,{\rm T}}(t^*) \equiv \frac{1}{2}\frac{\rm d}{{\rm d}t^*}\sigma_i^2 \tag{18}$$

Figure 18 shows the time development of the turbulent diffusivity in the streamwise direction, $\hat{\Gamma}_{x,{\rm T}}(t^*)$. For $z_{inj}^+ = 10$ and 100, $\hat{\Gamma}_{x,{\rm T}}(t^*)$ increases with the Stokes number from case A to D. For $z_{inj}^+ = 2$ instead $\hat{\Gamma}_{x,{\rm T}}(t^*)$ is not monotone with the Stokes number and is maximum in case C (St=1).

Figure 19 shows the time development of the turbulent diffusivity in the wall-normal direction, $\hat{\Gamma}_{z,{\rm T}}(t^*)$. Figure 19(a) shows that the peak $\hat{\Gamma}_{z,{\rm T}}(t^*)$ increases with Stokes number. This is due to the Lagrangian velocity autocorrelation (not shown) of larger particles decaying more slowly than for fluid points. Thus, large particles exhibit a greater time period of short time ($t \ll T_{x,{\rm L}}$) dispersion ($\propto t^2$). As a result, $\hat{\Gamma}_{z,{\rm T}}(t^*)$ for inertial particles will exceed that of fluid points for short times. A similar behavior was observed by Elghobashi & Truesdell (1992) in DNS of particle dispersion in isotropic turbulence. This argument does not hold for Figs. 19(b) and (c), as particles are moving in the viscous sublayer for short times. For very long times ($t^* > 80$), the fluid point turbulent diffusivity converges to $\hat{\Gamma}_{z,{\rm T}}(t^*) \approx 0.002$ independently of z_{inj}^+.

4 Conclusions

We have presented, for the first time, particle dispersion statistics obtained by performing DNS of a particle-laden spatially developing turbulent boundary layer using an Eulerian-Lagrangian approach.

We showed that the streamwise and wall-normal displacement of the particle cloud centroid decreases with increasing Stokes number independently of z_{inj}^+. This was explained by particles tendency to preferentially accumulate in the viscous sublayer for increasing Stokes number. Flow visualizations showed that St= 5 particles have peak concentration in the viscous sublayer whereas fluid points have nearly uniform concentration profiles.

The dispersion characteristics of inertial particles was then computed by measuring the mean-square displacment, $\sigma_i^2(t^*)$, and the turbulent diffusivity, $\hat{\Gamma}_{i,{\rm T}}(t^*)$. We found that streamwise dispersion for fluid points is fundamentally different from that of inertial particles. Due to the trapping of inertial particles in the viscous sublayer, cases C and D exhibit nearly $\propto t^{5/2}$ dispersion in the streamwise direction, whereas cases A and B exhibit nearly $\propto t^{5/3}$ dispersion, which is different than streamwise dispersion in homogeneous turbulent shear flow ($\propto t^3$). For cases C and D, the particle cloud was separated into two components, one which was trapped in the viscous sublayer, and the other traveling in the outer flow with mean velocity $\approx 0.8U_\infty$.

For all cases, the wall-normal dispersion, $\sigma_z^2(t^*)$, is approximately $\propto t$ for $t^* > 30$. Also, for particles released in the log-layer, $\sigma_z^2(t^*)$ was found to be nearly independent of the Stokes number.

Finally, we showed excellent agreement with Batchelor (1964) for the mean displacement of fluid points in the streamwise and wall-normal direction. Because the Lagrangian similarity hypothesis requires particles to remain in the log-layer, Batchelor (1964) does not hold for long times. Also, we found that the lower time limit can be relaxed to $t > T_{x,\mathrm{L}}$ for the time needed for the particles to lose memory of their initial conditions.

References

AHMED, A. M. & ELGHOBASHI, S. 2001 Direct numerical simulation of particle dispersion in homogeneous turbulent shear flows. *Phys. Fluids* **13**, 3346.

BATCHELOR, G. K. 1964 Diffusion from sources in a turbulent boundary layer. *Arch. Mech. Stosowanej* **16** (3), 661–670.

CAPORALONI, M., TAMPIERI, F., TROMBETTI, F. & VITTORI, O. 1975 Transfer of particles in nonisotropic air turbulence. *J. Atmos. Sci.* **32**, 565–568.

CERMAK, J. E. 1963 Lagrangian similarity hypothesis applied to diffusion in turbulent shear flow. *J. Fluid Mech.* **15**, 49–64.

CHATWIN, P. C. 1968 The dispersion of a puff of passive contaminant in the constant stress region. *Q. Jl Roy. Met. Soc.* **94**, 350–360.

CORRSIN, S. 1959 Progress report on some turbulent diffusion research. *Adv. Geophys.* **6**, 161–164.

DEGRAAFF, D. B. & EATON, J. K. 2000 Reynolds-number scaling of the flat-plat turbulent boundary layer. *J. Fluid Mech.* **422**, 319–346.

ELGHOBASHI, S. E. & TRUESDELL, G.C. 1992 Direct simulation of particle dispersion in a decaying isotropic turbulence. *J. Fluid Mech.* **242**, 655–700.

FERRANTE, A. 2004 Reduction of skin-friction in a microbubble-laden spatially developing turbulent boundary layer over a flat plate. PhD thesis, University of California, Irvine.

FERRANTE, A. & ELGHOBASHI, S. E. 2004 A robust method for generating inflow conditions for direct simulations of spatially-developing turbulent boundary layers. *J. Comput. Phys.* **198**, 372–387.

LOWERY, P. S. & REYNOLDS, W. C. 1986 Numerical simulation of a spatially-developing, forces, plane mixing layer. Rep. TF-26. Stanford University.

LUND, T.S., WU, X. & SQUIRES, K.D. 1998 Generation of turbulent inflow data for spatially-developing boundary layer simulations. *Journal of Computational Physics* **140** (2), 233–258.

MARCHIOLI, C. & SOLDATI, A. 2002 Mechanisms for particle transfer and segregation in a turbulent boundary layer. *J. Fluid Mech.* **468**, 283–315.

MAXEY, M.R. & RILEY, J.J. 1983 Equation of motion for a small rigid sphere in a nonuniform flow. *Phys. Fluids* **26**, 883–889.

Morgan, B., Larsson, J., Kawai, S. & Lele, S. 2011 Improving low-frequency characteristics of recycling/rescaling inflow turbulence generation. *AIAA Journal* **49**, 582–597.

Pope, S. B. 2000 *Turbulent Flows*. Cambridge Univ. Press.

Poreh, M. & Cermak, J. E. 1964 Study of diffusion from a line source in a turbulent boundary layer. *Int. J. Heat Mass Transfer* **7**, 1083–1095.

Reeks, M. W. 1983 The transport of discrete particles in inhomogeneous turbulence. *J. Aerosol Sci.* **14**, 729–739.

Schlatter, P. & Örlü, R. 2010 Assessment of direct numerical simulation data of turbulent boundary layers. *J. Fluid Mech.* **659**, 116–126.

Schlatter, P., Örlü, R., Li, Q., Brethouwer, G., Frannson, J. H. M., Johansson, A. V., Alfredsson, P. H. & Henningson, D. S. 2009 Turbulent boundary layers up to $Re_\theta = 2500$ studied through simulation and experiment. *Phys. Fluids* **21**, 1–4.

Shlien, D. J. & Corrsin, S. 1976 Dispersion measurements in a turbulent boundary layer. *Int. J. Heat Mass Transfer* **19**, 285–295.

Soldati, A. & Marchioli, C. 2009 Physics and modelling of turbulent particle deposition and entrainment: Review of a systematic study. *Int. J. Multiphase Flow* **35**, 827–839.

Taylor, G. I. 1921 Diffusion by continuous movement. *Proc. Lond. Math. Soc* **20**, 196–212.

Yeung, P. K. 2002 Lagrangian investigation of turbulence. *Annu. Rev. Fluid Mech.* **34**, 114–142.
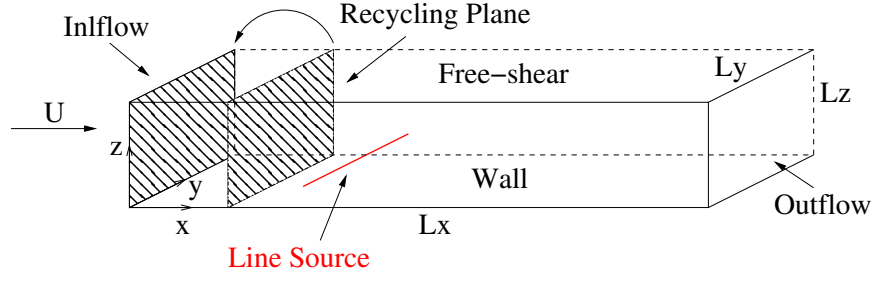
Figure 1: Schematic of the computational domain (not to scale).
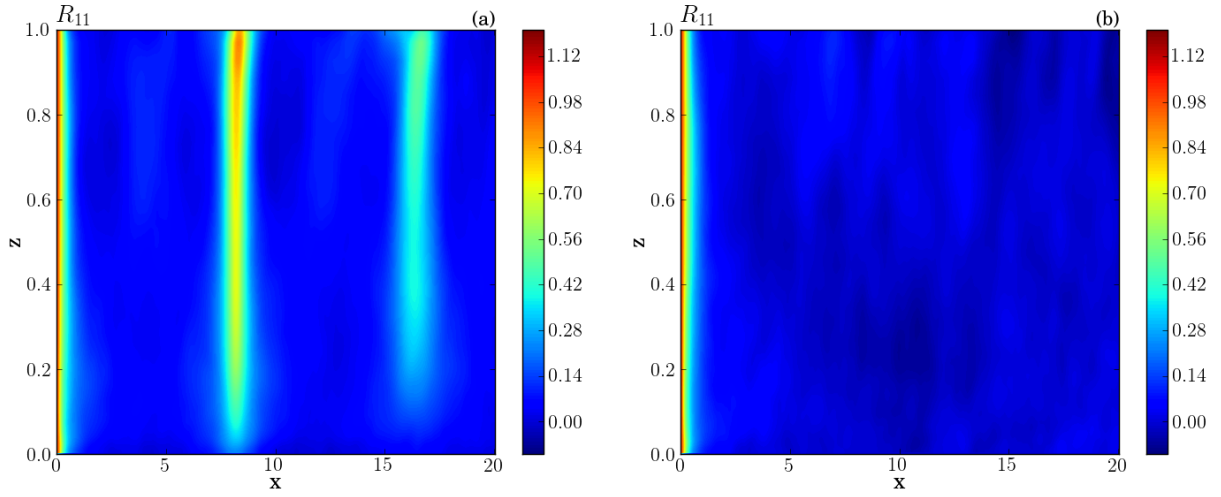
Figure 2: $x - z$ plane contours of the two-point streamwise velocity correlation, R_{11} (Eq. 5), computed using an inflow generation method (a) without dynamic reflection and (b) with dynamic reflection for case 3 (Table 3).
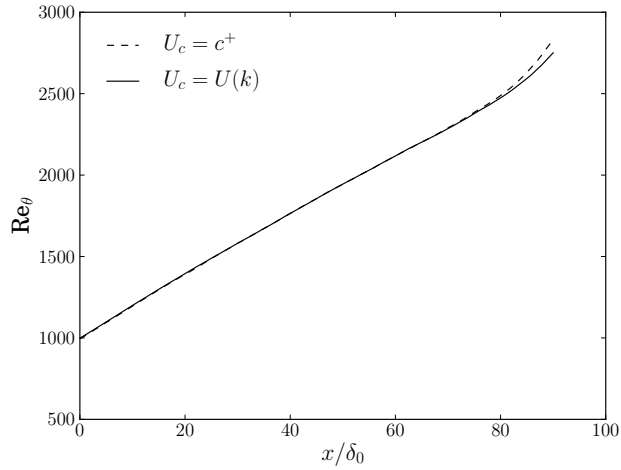
Figure 3: Momentum thickness Reynolds number, Re_θ, versus streamwise position, x.

12
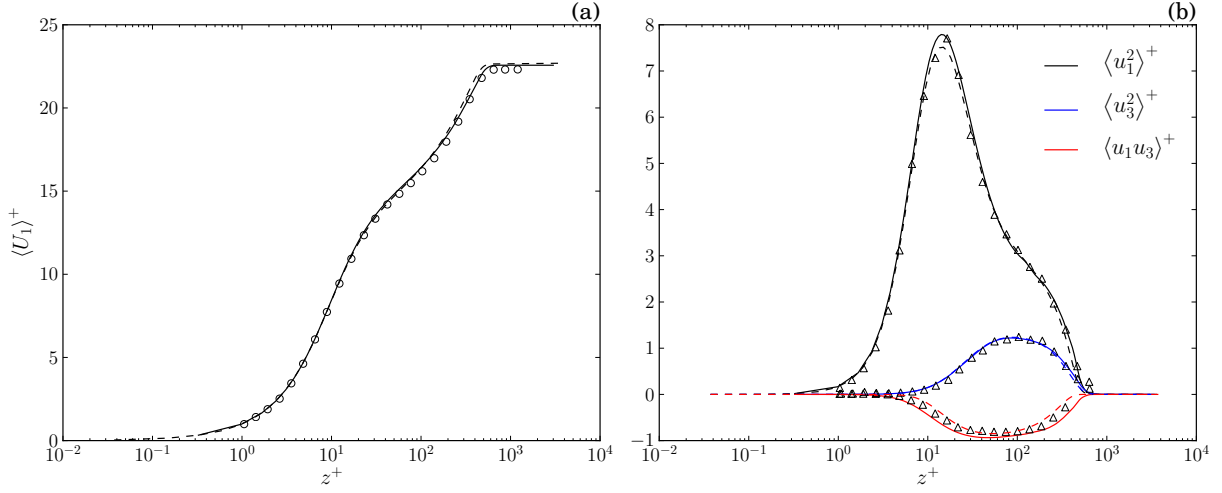
Figure 4: (a) Mean streamwise velocity profile and (b) Reynolds stress profiles. Present DNS at $Re_\theta = 1430$ (solid lines); experimental data of DeGraaff & Eaton (2000) at $Re_\theta = 1430$ (symbols); DNS data of Schlatter & Örlü (2010) at $Re_\theta = 1421$ (dashed lines).
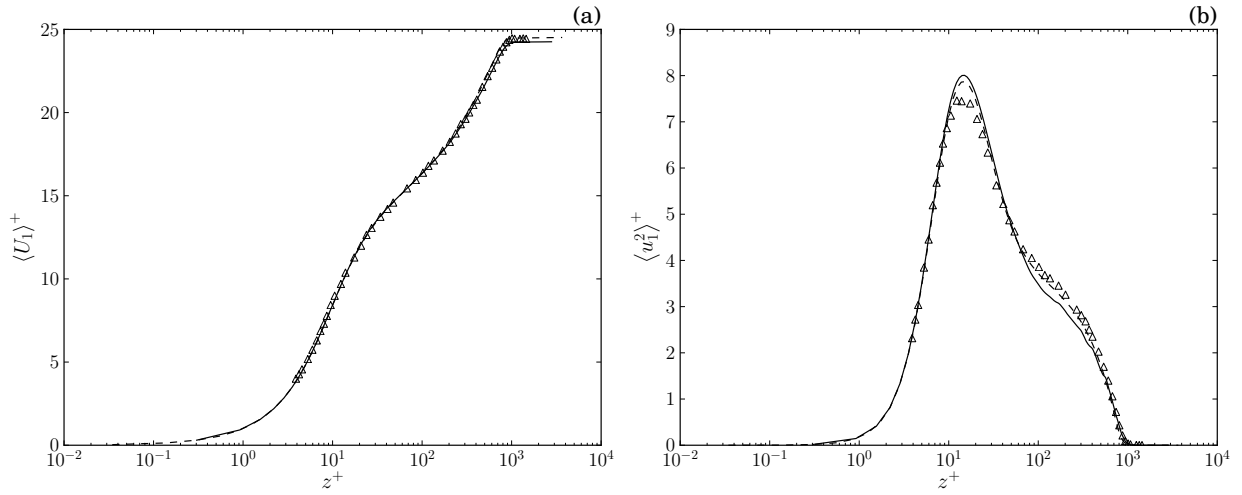
Figure 5: (a) Mean streamwise velocity profile and (b) normal Reynolds stress profile. Present DNS at $Re_\theta = 2541$ (solid lines); experimental data of Schlatter *et al.* (2009) at $Re_\theta = 2541$ (symbols); DNS data of Schlatter & Örlü (2010) at $Re_\theta = 2537$ (dashed lines).
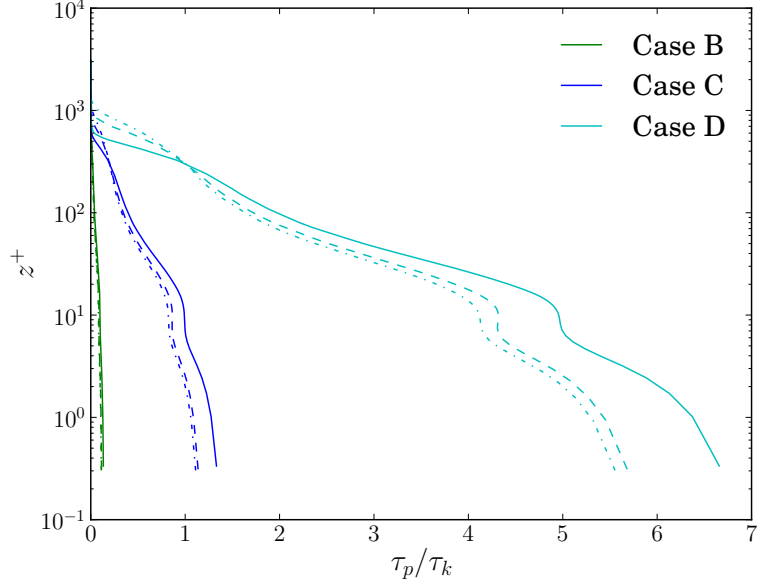
Figure 6: Particle Stokes number (τ_p/τ_k) versus z^+ for case B, C, and D at three x-positions; $x = 10\delta_0$ (solid lines), $x = 50\delta_0$ (dashed lines), and $x = 80\delta_0$ (dot-dashed lines).
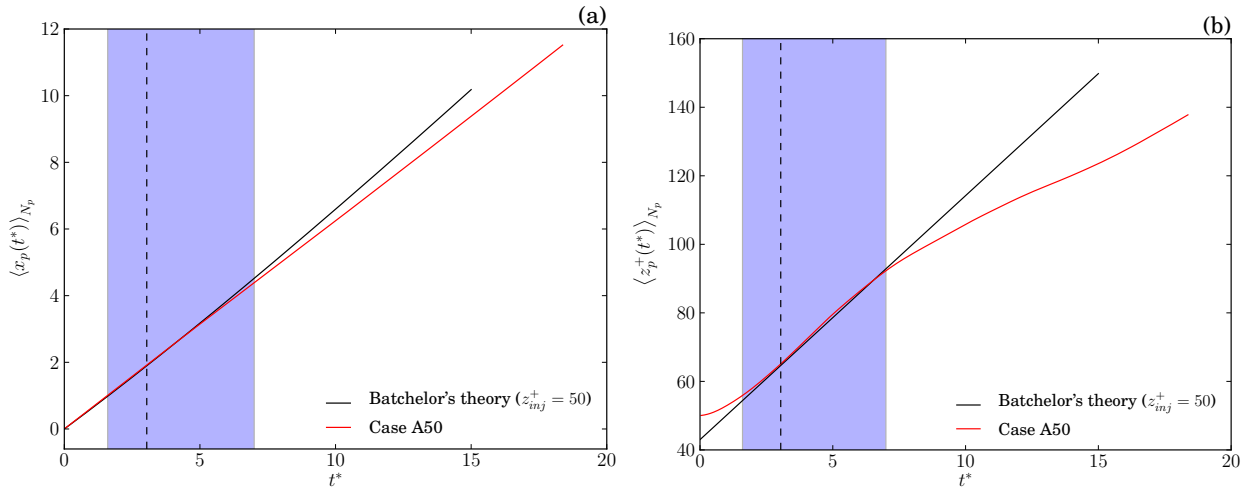
Figure 7: Time development of the mean displacement of fluid points from present DNS and Batchelor (1964) theory. (a) Streamwise direction $\langle x_p(t^*)\rangle_{N_p}$ and (b) wall-normal direction $\langle z_p^+(t^*)\rangle_{N_p}$. The blue area represents the time range in which Batchelor's theory shows good agreement and the dashed line is t_1.
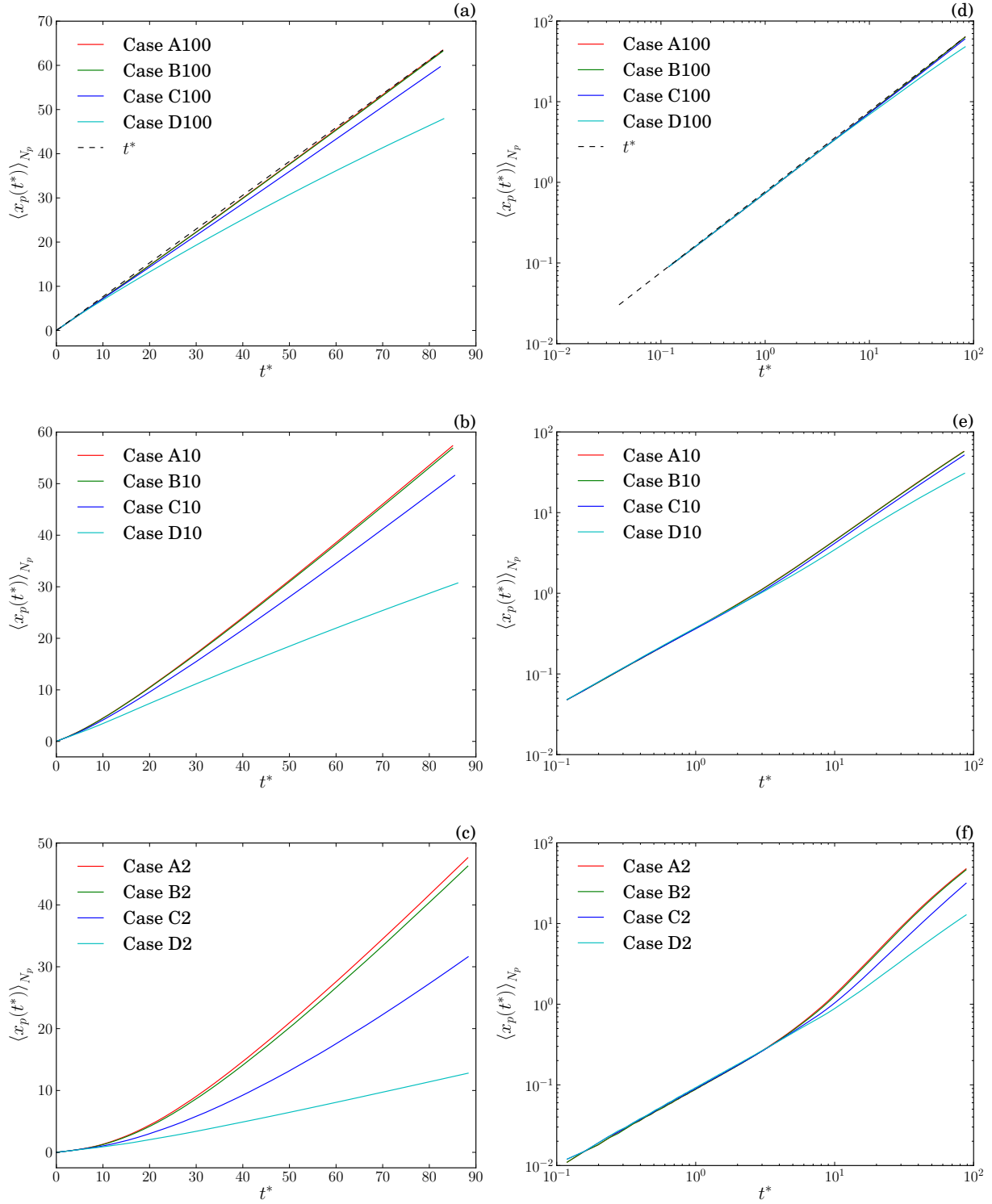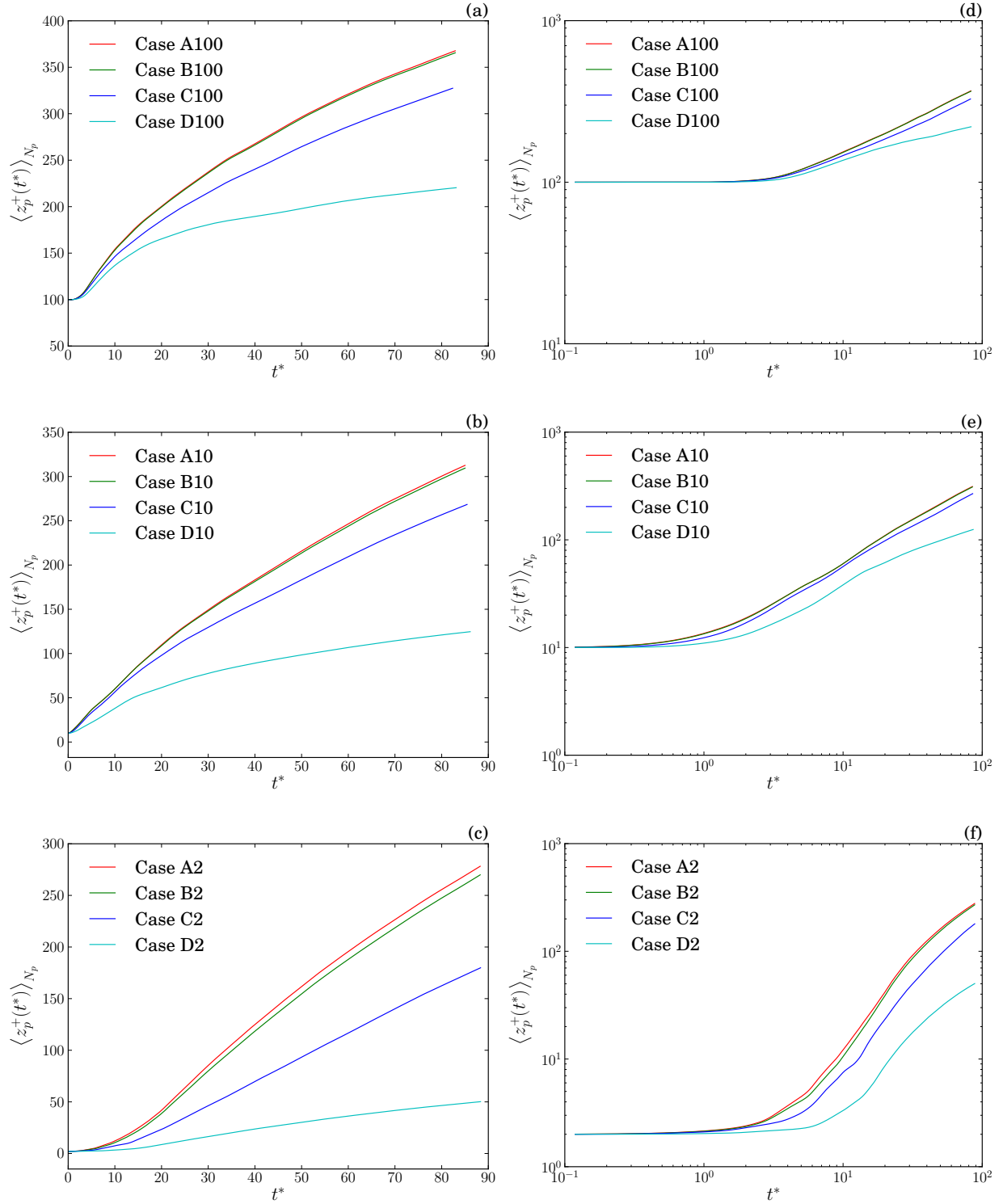
Figure 8: Time development of the streamwise location of the particle cloud centroid, $\langle x_p(t^*) \rangle_{N_p}$ Eq. (13), for particles released at $z_{inj}^+ = 100$, 10, and 2. Lin-lin plot (left column); log-log plot (right column).
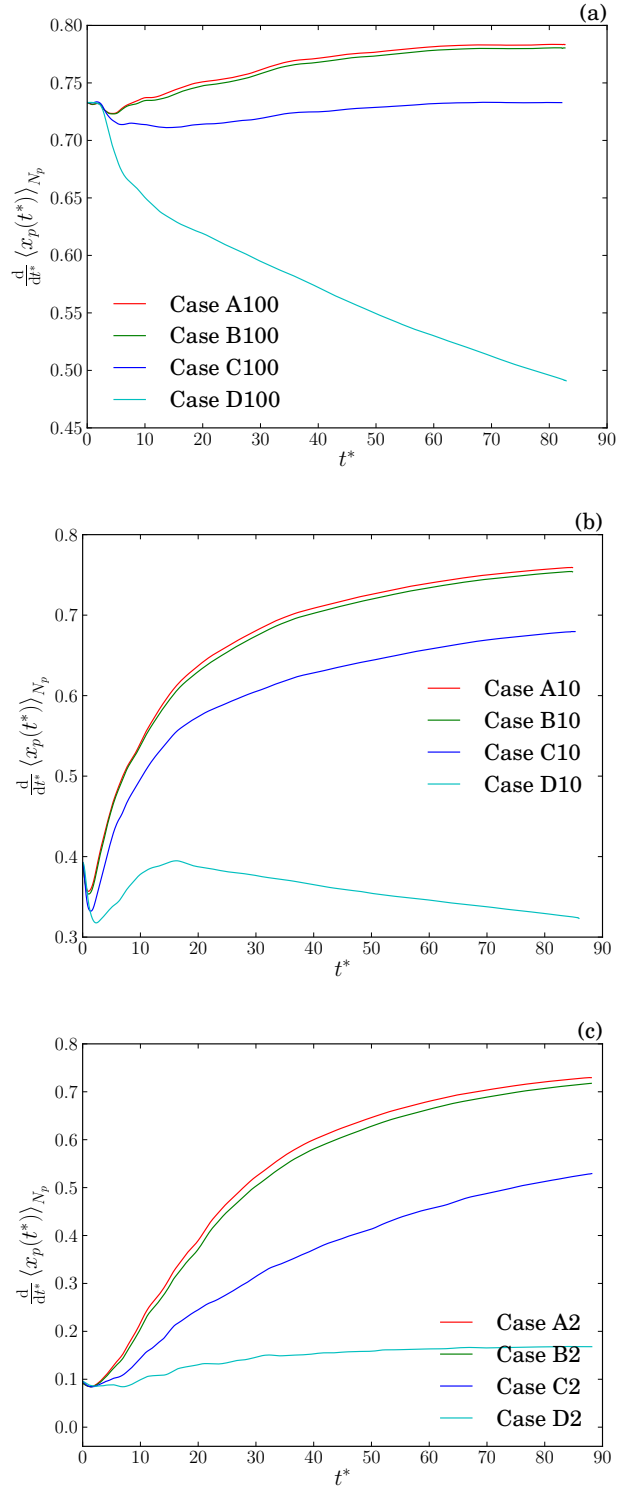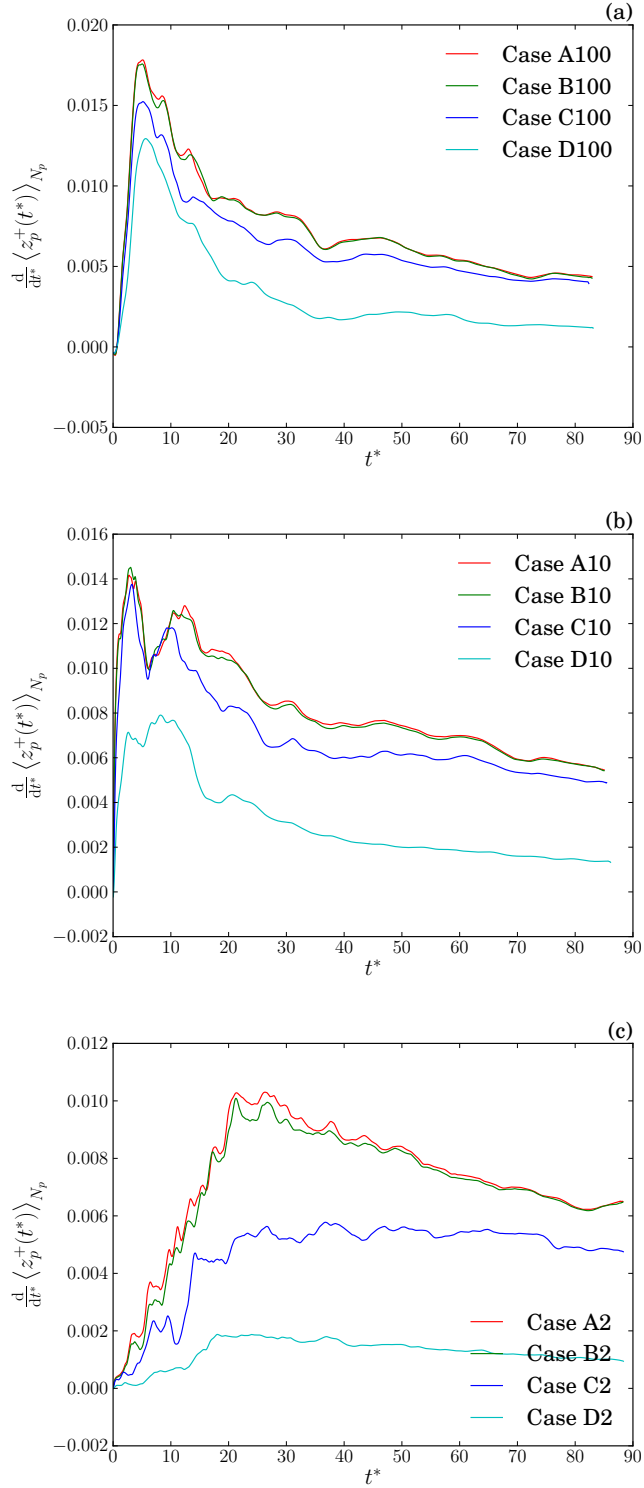
Figure 9: Time development of the streamwise velocity of the particle cloud centroid, $\frac{\mathrm{d}}{\mathrm{d}t^*}\langle x_p(t^*)\rangle_{N_p}$, for particles released at $z_{inj}^+ = 100$, 10, and 2.
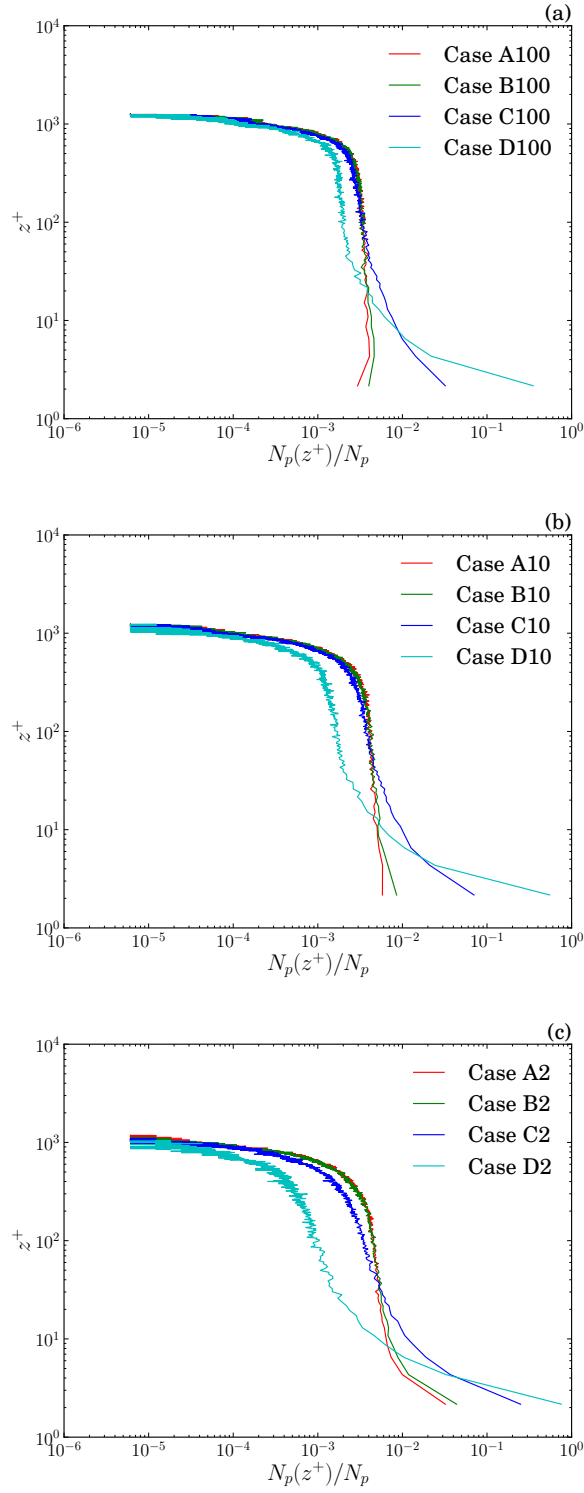
Figure 10: Instantaneous profile of particle concentration, $N_p(z^+)/N_p$, as a function of z^+ normalized by the total number of particles in the compuatational domain, N_p. Profiles are taken at $t^* = 84.0$ for particles released at $z^+_{inj} = 100$, 10, and 2.
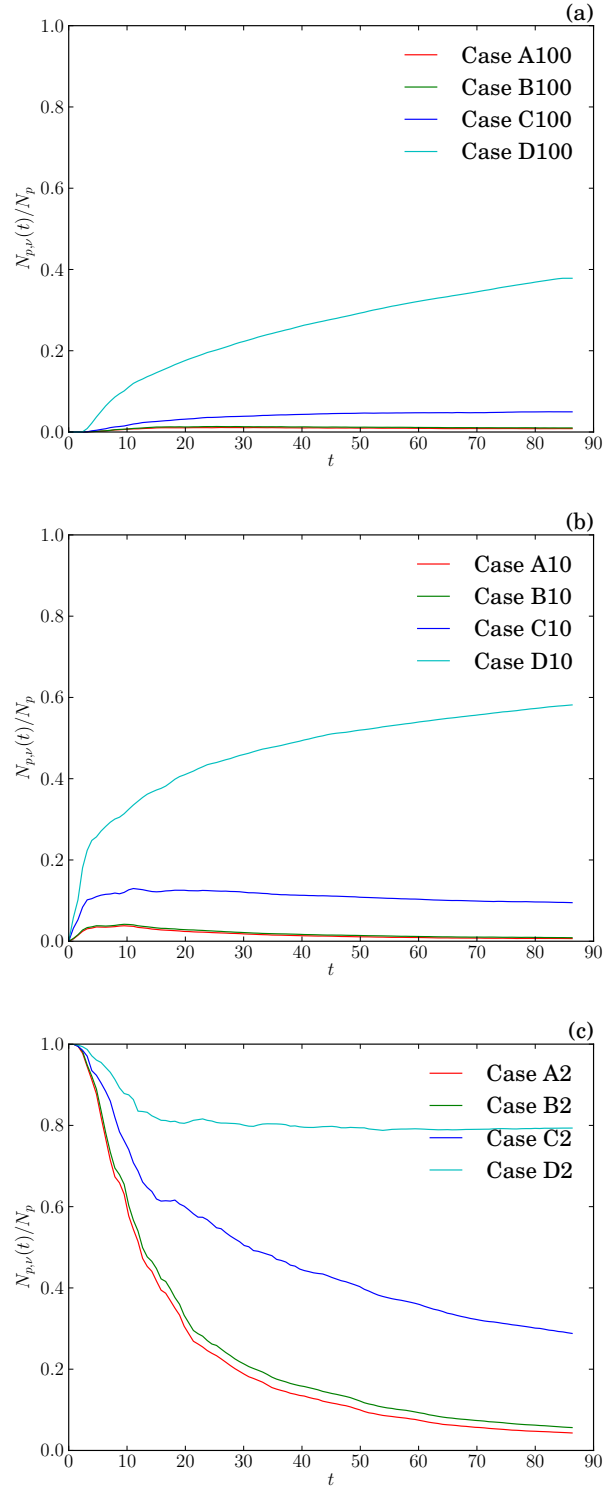
Figure 11: Time development of the number of particles in the viscous sublayer ($0 < z^+ < 5$) normalized by the total number of particles, $N_{p,\nu}(t)/N_p$, for particles released at $z^+_{inj} = 100$, 10, and 2.

Figure 12: Time development of the wall-normal location of the particle cloud centroid, $\langle z_p^+(t^*) \rangle_{N_p}$ Eq. (13), for particles released at $z_{inj}^+ = 100$, 10, and 2. Lin-lin plot (left column); log-log plot (right column).
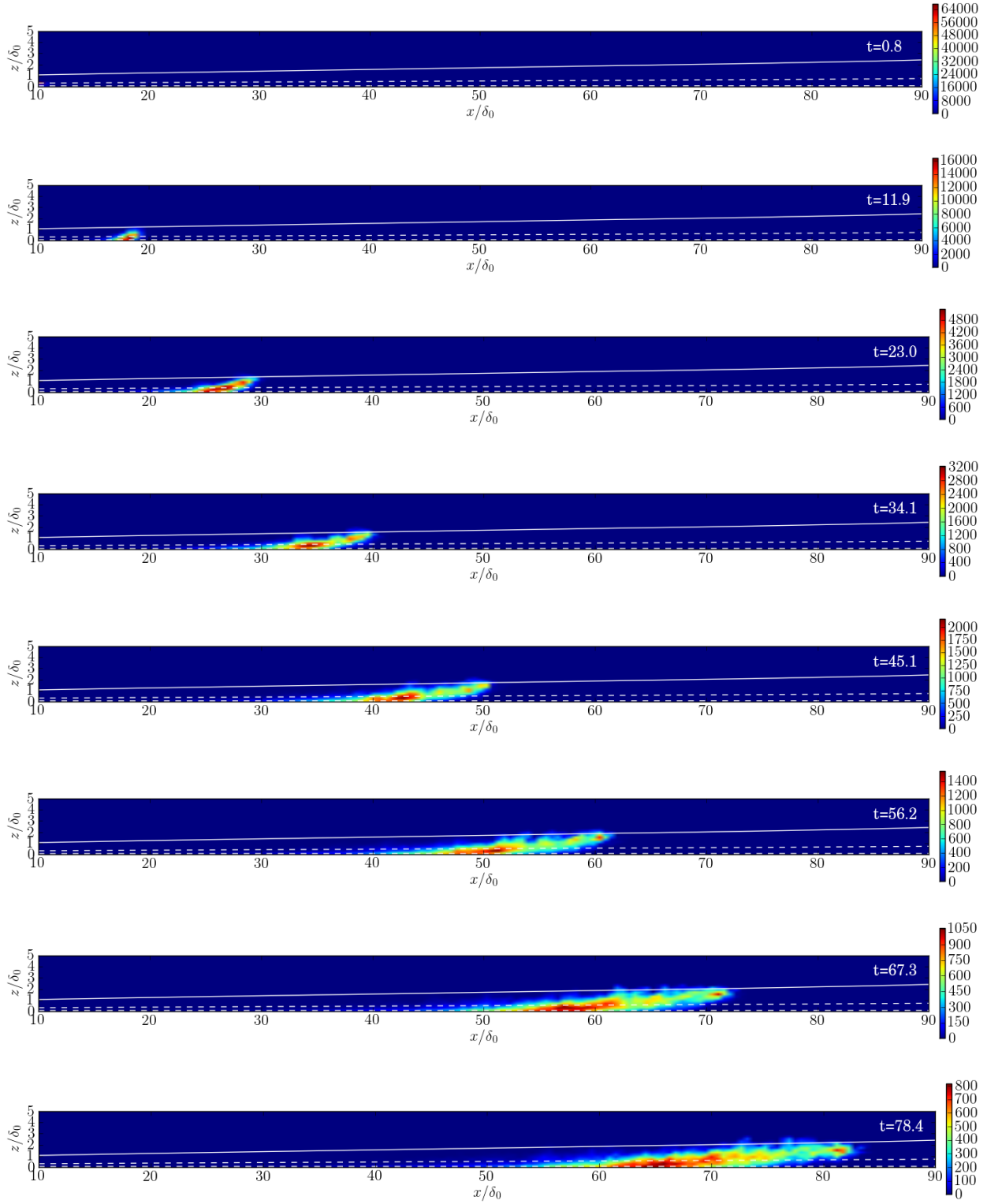
Figure 13: Time development of the wall-normal velocity of the particle cloud centroid, $\frac{\mathrm{d}}{\mathrm{d}t^*}\langle z_p^+(t^*)\rangle_{N_p}$, for particles released at $z_{inj}^+ = 100$, 10, and 2.
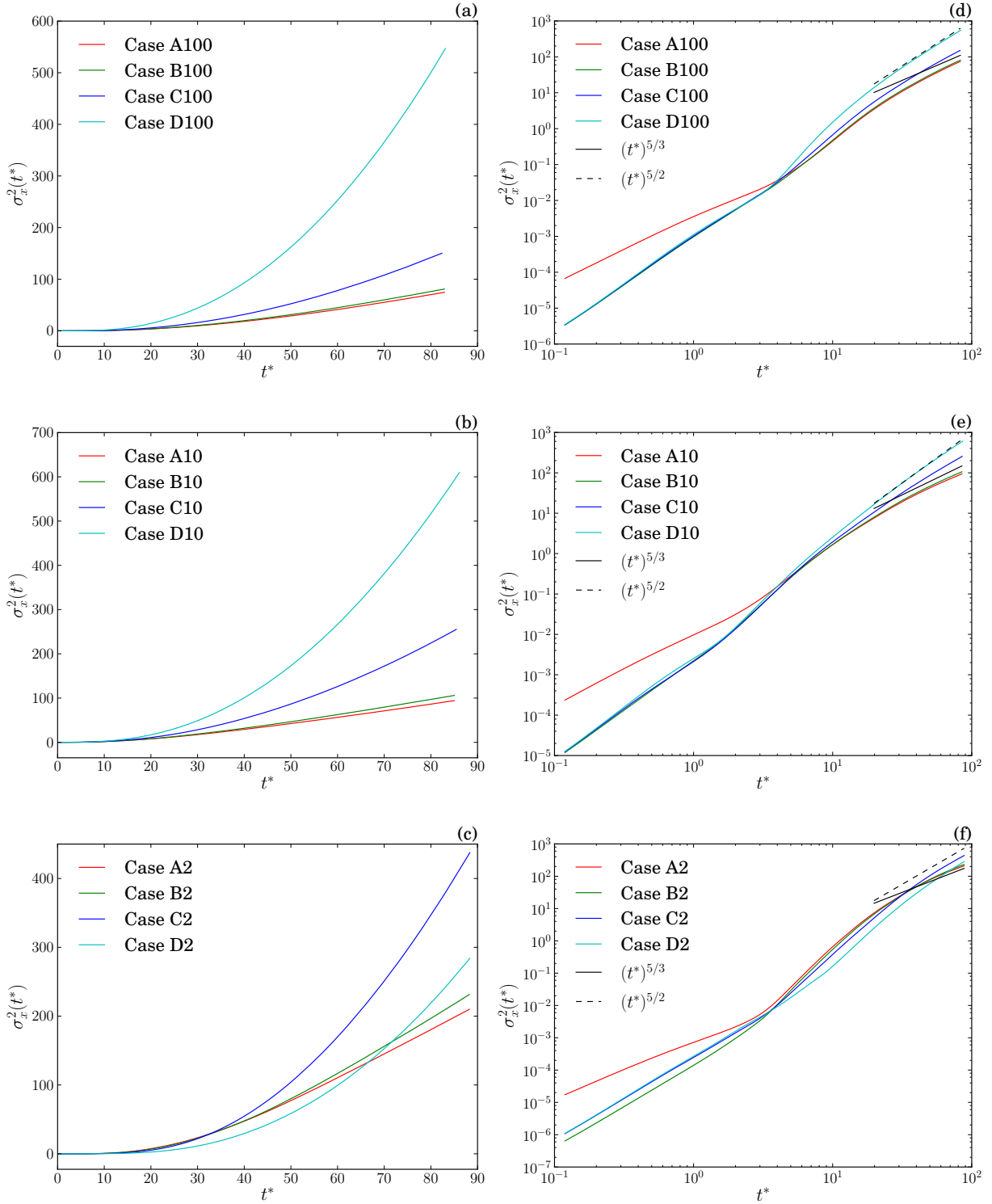
Figure 14: Time development of the streamwise dispersion, σ_x^2 Eq. (17), for particles released at $z_{inj}^+ = 100$, 10, and 2. Lin-lin plot (left column); log-log plot (right column).
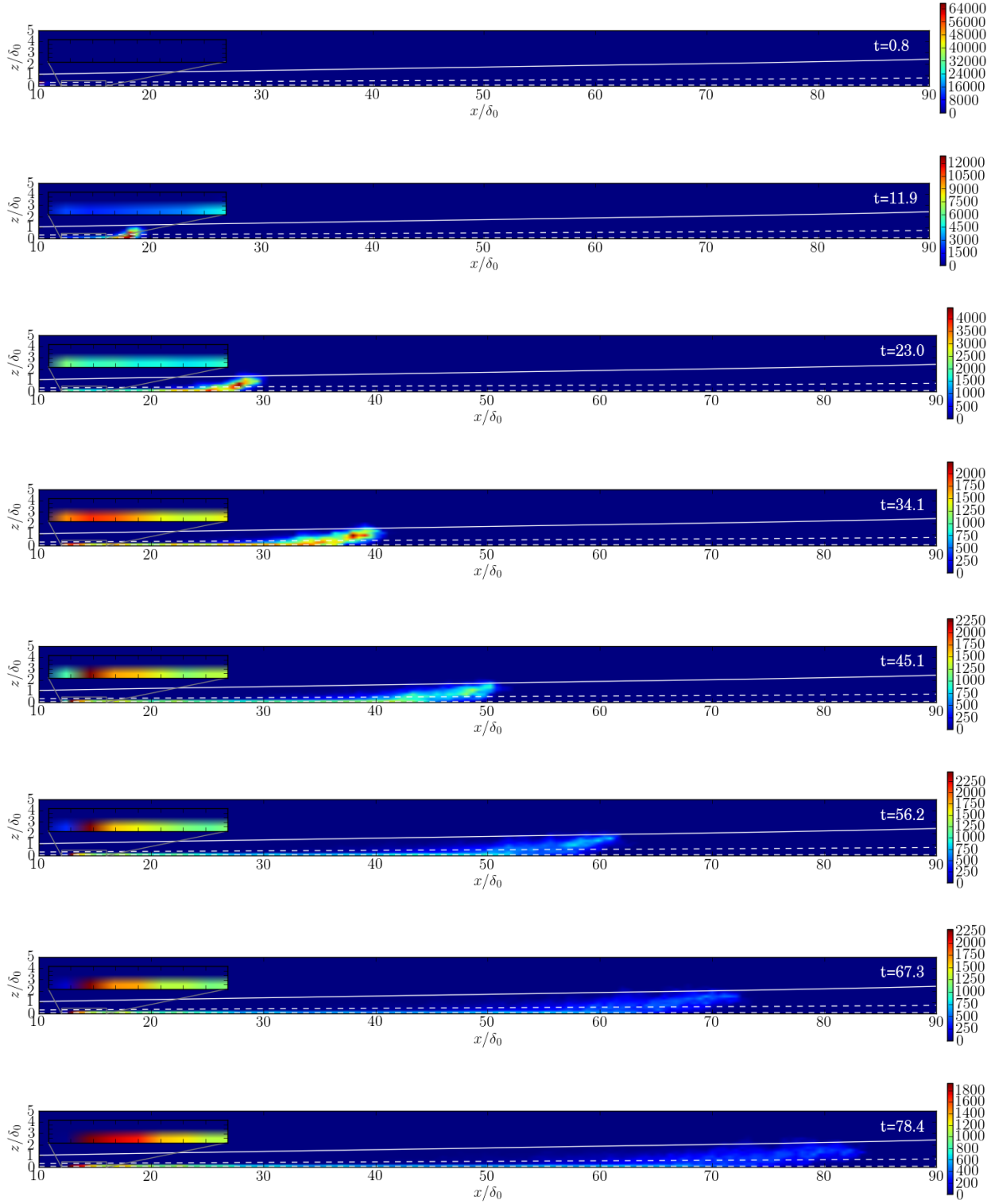
Figure 15: Instantaneous color contours of the number of particles summed in the spanwise direction for case A100 at times $t = 0.8, \ldots, 78.4$; boundary layer thickness, $\delta(x)$, (solid white line); and lower and upper boundaries of the log-layer ($z = 30\delta_\nu(x)$ and $z = 0.3\delta(x)$) (dashed white lines).
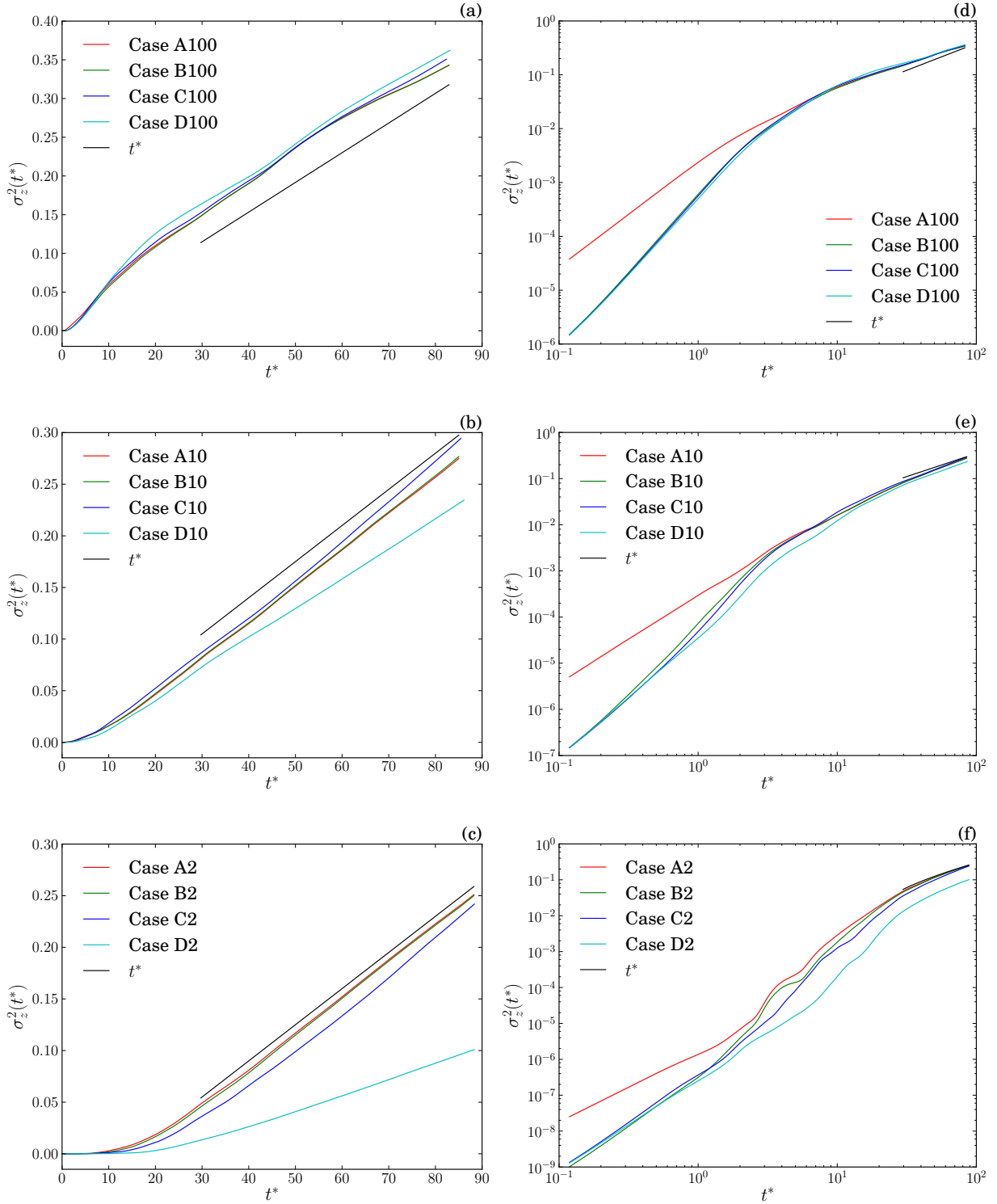
Figure 16: Instantaneous color contours of the number of particles summed in the spanwise direction for case D100 at times $t = 0.8, \ldots, 78.4$; boundary layer thickness, $\delta(x)$, (solid white line); and lower and upper boundaries of the log-layer ($z = 30\delta_\nu(x)$ and $z = 0.3\delta(x)$) (dashed white lines).

Figure 17: Time development of the wall-normal dispersion, σ_z^2 Eq. (17), for particles released at $z_{inj}^+ = 100$, 10, and 2. Lin-lin plot (left column); log-log plot (right column).
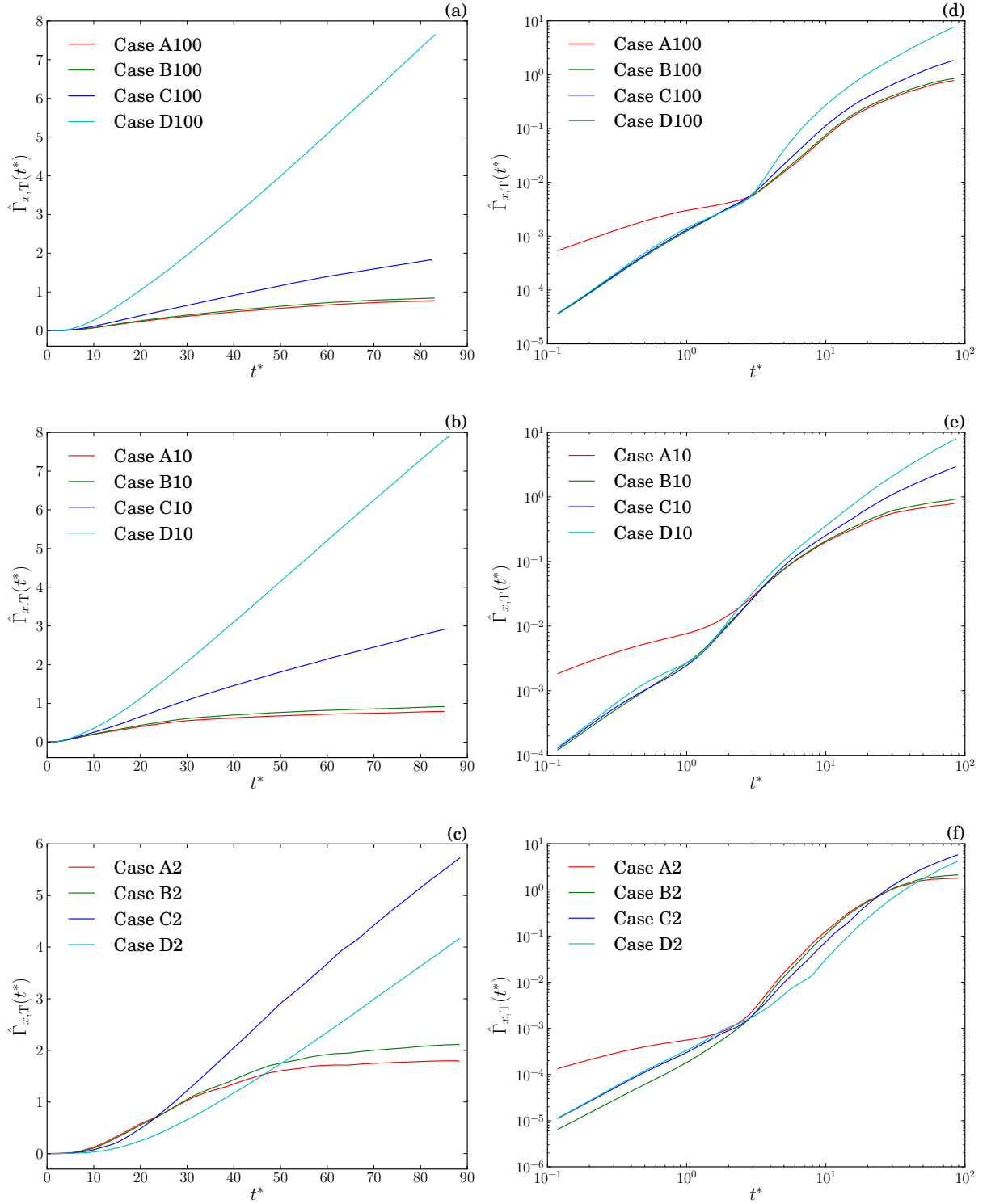
24

Figure 18: Time development of the Lagrangian turbulent diffusivity, $\widehat{\Gamma}_{x,\mathrm{T}}(t^*)$ Eq. (18), in the streamwise direction for particles released at $z_{inj}^+ = 100, 10,$ and 2. Lin-lin plot (left column); log-log plot (right column).
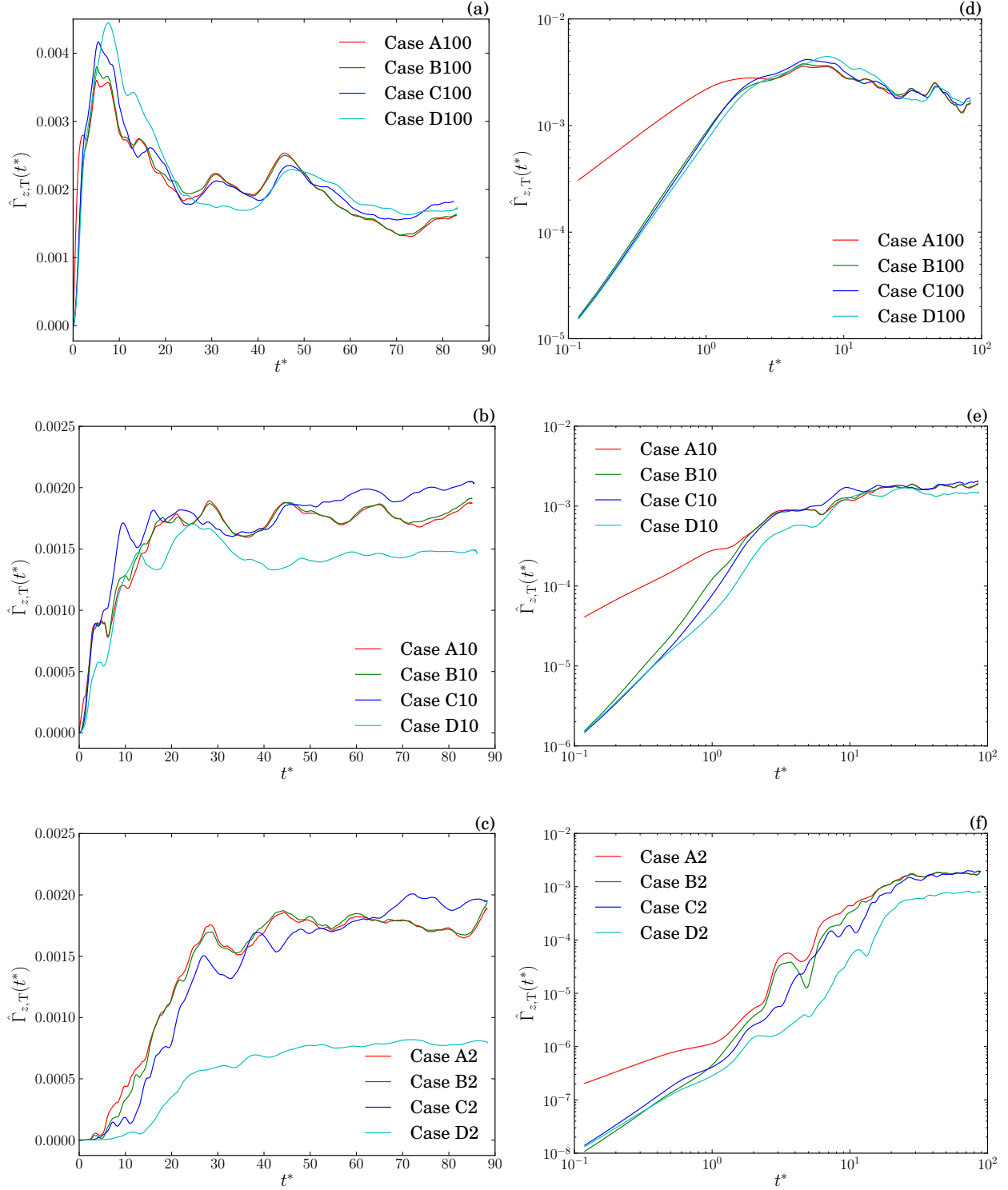
Figure 19: Time development of the Lagrangian turbulent diffusivity, $\widehat{\Gamma}_{z,\mathrm{T}}(t^*)$ Eq. (18), in the wall-normal direction for particles released at $z_{inj}^+ = 100$, 10, and 2. Lin-lin plot (left column); log-log plot (right column).